PNAS RESEARCH ARTICLE | PHYSICS

Visualizing the interplay of Dirac mass gap and magnetism at nanoscale in intrinsic magnetic topological insulators

Mengke Liu[a], Chao Lei[a], Hyunsue Kim[a], Yanxing Li[a], Lisa Frammolino[a], Jiaqiang Yan[b], Allan H. Macdonald[a,1], and Chih-Kang Shih[a,1]

Contributed by Allan H. MacDonald; received May 31, 2022; accepted September 2, 2022; reviewed by Abhay Pasupathy and Di Xiao

In intrinsic magnetic topological insulators, Dirac surface-state gaps are prerequisites for quantum anomalous Hall and axion insulating states. Unambiguous experimental identification of these gaps has proved to be a challenge, however. Here, we use molecular beam epitaxy to grow intrinsic $MnBi_2Te_4$ thin films. Using scanning tunneling microscopy/spectroscopy, we directly visualize the Dirac mass gap and its disappearance below and above the magnetic order temperature. We further reveal the interplay of Dirac mass gaps and local magnetic defects. We find that, in high defect regions, the Dirac mass gap collapses. *Ab initio* and coupled Dirac cone model calculations provide insight into the microscopic origin of the correlation between defect density and spatial gap variations. This work provides unambiguous identification of the Dirac mass gap in $MnBi_2Te_4$ and, by revealing the microscopic origin of its gap variation, establishes a material design principle for realizing exotic states in intrinsic magnetic topological insulators.

magnetic topological insulator | Dirac mass gap | STM/STS | topological phase transition

Significance

Intrinsic magnetic topological insulators (MTIs) $MnBi_2Te_4$ have recently emerged as a new frontier of topological quantum materials. Theoretical predicted exotic quantum phases of its thin-film form, such as Chern and axion insulator states, both have Dirac mass gaps in their surface states. However, direct observation of the Dirac mass gap has proved challenging. Here, we report the direct observation of the Dirac mass gap. We further reveal microscopically the essential role of native magnetic antisite defects in controlling the formation of the Dirac mass gap. Our work provides unambiguous evidence of a Dirac mass gap in $MnBi_2Te_4$ thin film and identifies magnetic defects as an important parameter in designing the topological quantum material.

In magnetic topological insulators (MTIs), time-reversal symmetry breaking opens a surface-state Dirac mass gap that is a prerequisite for realizing quantum anomalous Hall (QAH) and axion insulator ground states (1–3). QAH states support spin-momentum locked dissipationless edge states that hold great promise in advancing electronic and spintronic device applications. Early materials design was based on doping topological insulators with magnetic elements (4, 5); however, dopant disorder (6, 7) is significant and considered to be the main cause for quantized edge states being observed only at extremely low temperatures, ∼30 mK in chromium-doped $(Bi,Sb)_2Te_3$ (5). Recently, a new family of intrinsic MTIs based on layered van der Waals material $MnBi_2Te_4$ has emerged, in which an ordered Mn magnetic layer is incorporated stoichiometrically in the middle of each van der Waals layer (8–14), suppressing the disorder effect. Indeed, the QAH effect has been observed in $MnBi_2Te_4$ at a significantly higher temperature of 1.4 K (15). However, the QAH effect is not always observed, even in samples that appear similar (16–20). Moreover, observations of the Dirac mass gap, a prerequisite for the QAH effect and a direct consequence of exchange coupling between the Dirac surface state and the spontaneous magnetization (21, 22), has proven to be challenging and remained unclear (9, 23–30). Given the significant fundamental and application interest in this system, addressing the elusive nature of the Dirac mass gap becomes ever more critical.

Current bulk $MnBi_2Te_4$ samples are known to be heavily degenerate n-type, with Fermi level (E_F) located deeply inside the conduction band (9, 23–26). As a result, short Dirac fermion lifetimes smear gap signatures. Besides, defects distribution inhomogeneity can complicate the magnetic order (30–32) and impact the exchange-gap distribution (6, 32–37). Spatial fluctuations of chemical potential and another chemical composition mixing, such as Bi_2Te_3 and $MnTe_2$ (16, 17, 38), further entangle the electronic structure and complicate the gap observation. Thus, to properly address the nature of Dirac mass gap, a microscopic characterization based on intrinsic samples with Fermi level lying within the Dirac gap is crucial.

Here, we achieve layer-by-layer growth of $MnBi_2Te_4$ thin film on high-oriented pyrolytic graphite (HOPG) and graphene substrate using molecular beam epitaxy (MBE). Furthermore, we control the defect concentration such that E_F lies inside the Dirac gap. Using *in situ* scanning tunneling microscopy/spectroscopy (STM/S), we directly observed the Dirac mass gap and its variation as a function of film thickness and the magnetic antistites concentrations. We found that, in high defect regions, the Dirac mass gap collapses. To understand these phenomena, we combine *ab initio* supercell calculation with the coupled Dirac cone model to account for the effect of magnetic antistites defects and demonstrate the Dirac mass gap fragility to antisites. Our calculation predicts maximum antisite densities for observing the QAH effect. This work provides unambiguous evidence for the presence of a Dirac mass gap in intrinsic MTI and reveals

Author contributions: M.L. and C.-K.S. designed research; M.L., C.L., H.K., Y.L., L.F., and C.-K.S. performed research; J.Y. contributed new reagents/analytic tools; M.L., C.L., H.K., A.H.M., and C.-K.S. analyzed data; and M.L., C.L., A.H.M., and C.-K.S. wrote the paper.

Reviewers: A.P., Columbia University; and D.X., University of Washington.

Competing interest statement: We acknowledge that J.Y. has coauthored papers with both reviewers. J.Y. developed the protocol of flux growth of MnBi2Te4 single crystals, and this protocol has been widely used by the community to produce high-quality single crystals of $MnBi_2Te_4$ and related compounds. In this work, $MnBi_2Te_4$ single crystals provided by J.Y. have been used to reveal the contrasting behaviors between bulk single crystals and MBE-grown ultra-thin films.

[1]To whom correspondence may be addressed. Email: macdpc@physics.utexas.edu or shih@physics.utexas.edu.

This article contains supporting information online at http://www.pnas.org/lookup/suppl/doi:10.1073/pnas.2207681119/-/DCSupplemental.

Published October 10, 2022.

the microscopic origin of the gap variation. It further establishes magnetic defect as a critical tuning knob in controlling the topological phases of MTI for QAH and axion insulator–based device applications.

Bulk Crystals versus MBE-Grown Thin Films

$MnBi_2Te_4$ is a layered van der Waals material consisting of Te-Bi-Te-Mn-Te-Bi-Te septuple layers (SLs), in which the Mn atomic layer is coupled ferromagnetically within the SL and antiferromagnetically with neighboring SLs. The lattice illustration shown in Fig. 1*A* includes two commonly observed native defects, Mn_{Bi} and Bi_{Te} antisites. STM images taken on the cleaved bulk crystals (Fig. 1*B*) show ∼5% Mn_{Bi} antisites, which appear as dark triangular depressions (39), and ∼0.2% of Bi_{Te} antisites, which appear as bright circular protrusions (39). The abundance of the Bi_{Te} antisites is related to the Te content during the growth (40). The broad background fluctuation may reflect an inhomogeneous distribution of the Bi_{Mn} antisite, the most common n-type dopant (40), located at the Mn layer and is too far from the surface to be directly imaged by STM. But its high concentration is expected from the internal strain energy in the middle Mn layer (40) and can be inferred from the heavily degenerate n-type nature of the sample. As shown in Fig. 1*C*, we find that E_F is 0.28 eV above the Dirac point in bulk samples, consistent with previous angle-resolved photoemission spectroscopic results (9, 23–25). However, the Dirac gap signature is smeared and difficult to quantify.

We succeed in growing $MnBi_2Te_4$ thin films on the HOPG and the graphene substrates. The STM/S results reported here are primarily carried out on samples grown on HOPG substrate. A typical STM image of our MBE-grown $MnBi_2Te_4$ flakes, shown in Fig. 1*D*, demonstrates SL-by-SL growth of high-quality $MnBi_2Te_4$ thin film. A topographic section across the flakes (Fig. 1*E*) allows us to determine the thickness in terms of the number of SLs. This thickness determination is crucial because it eliminates the possibility of Bi_2Se_3 or $MnTe_2$ intermixing, which would lead to different layer thicknesses (additional topographic images of MBE grown samples can be found in *SI Appendix*, Fig. S1). Fig. 1 *D*, *Inset* shows the corresponding atomic image, exhibiting ∼4% of Mn_{Bi} antisites and no bright Bi_{Te} antisites. The disappearance of Bi_{Te} antisites is due to a Te-rich growth ambient, which also reduces the Bi_{Mn} antisites (40). Most importantly, in the ultra-thin regime, the internal energy in the Mn layer may not yet build up significantly, thus delaying the strain compensation effect through Bi_{Mn} antisites (40). The clean and flat background of the atomic image reflects a considerably reduced amount of Bi_{Mn} antisites. The SL-by-SL MBE growth of $MnBi_2Te_4$ films with low defect density we report provides access to the rich electronic properties of $MnBi_2Te_4$ thin films.

Direct Observation of Dirac Mass Gaps

We start with the 4-SL film, thick enough that its topological surface state is well developed. Fig. 2*A* shows a typical tunneling spectrum acquired at 4.3 K at a relatively high setpoint bias of 0.6 V. In this spectrum, there exists a sizeable low-conductance bias range from −0.3 V to +0.4 V, marked by the blue and orange arrows. This low-conductance region is due to a significantly reduced density of states (DOS). We find that, with a lower setpoint bias, as shown in Fig. 2*B*, for which the tip-to-sample distance is reduced, states near E_F can be well resolved. The behavior of bias-dependent tip-to-sample distance can be found in *SI Appendix*, Fig. S2, and the tunneling junction characteristics (barrier height) at different biases can be found in *SI Appendix*, Fig. S3. In Fig. 2*B*, which focuses on states near the Fermi energy, one can observe a clear exchange gap of ∼120 meV, with E_F located 20 meV below the conduction band edge.

We further carried out the STS measurement at 77 K, a temperature above the Neel temperature. At a high setpoint bias

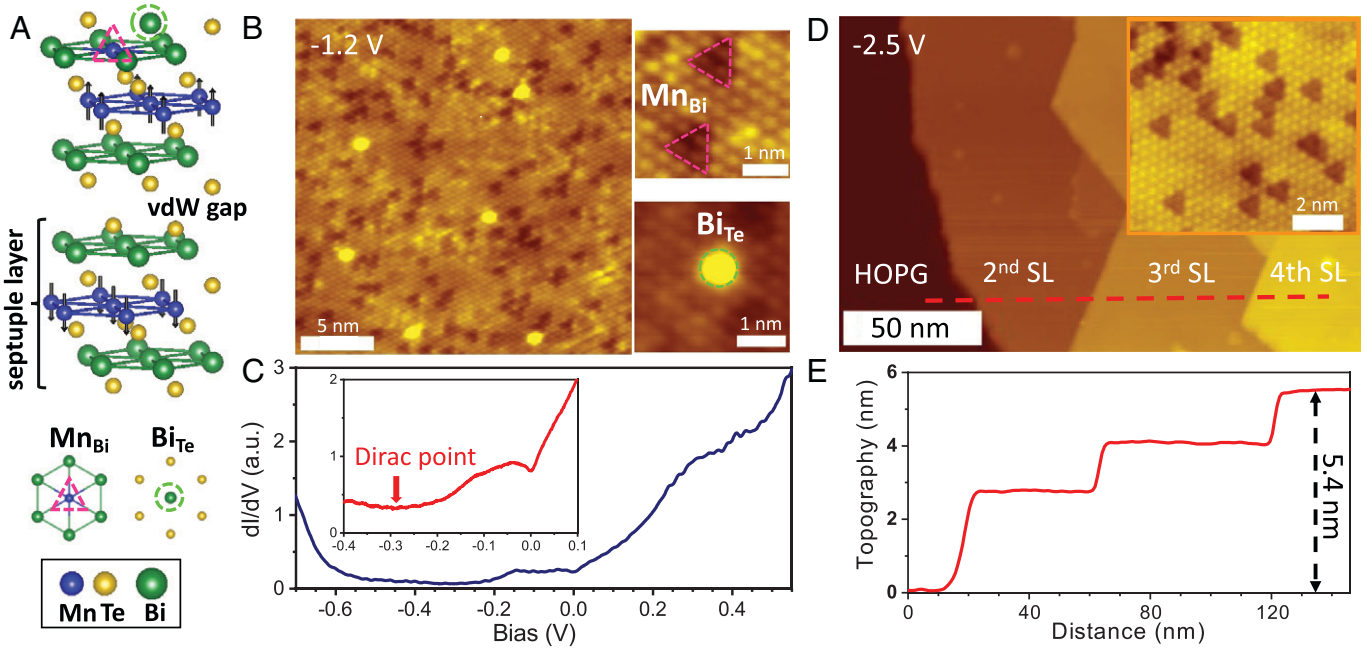

Fig. 1. Bulk crystals versus MBE-grown thin films. (*A*) Crystal structure of $MnBi_2Te_4$. The black arrows illustrate the intralayer ferromagnetic and interlayer antiferromagnetic coupling. Cleave plane happens at the van der Waals gap. Mn_{Bi} and Bi_{Te} antisite defects are outlined with a pink triangle and green circle. (*B*) Atomic image taken on Te truncated bulk $MnBi_2Te_4$ surface. Examples of Mn_{Bi} and Bi_{Te} antisites are outlined by pink triangles and green circles. (*C*) STS taken on bulk $MnBi_2Te_4$ surface. *Inset* red curve shows zoom-in bias range. The red arrow marks the Dirac point. (*D*) Topographic image taken on MBE-grown $MnBi_2Te_4$. *Inset* shows its atomic image. (*E*) Topographic cross-section along the red dashed line in *D* shows the thickness of each SL is 1.35 nm.

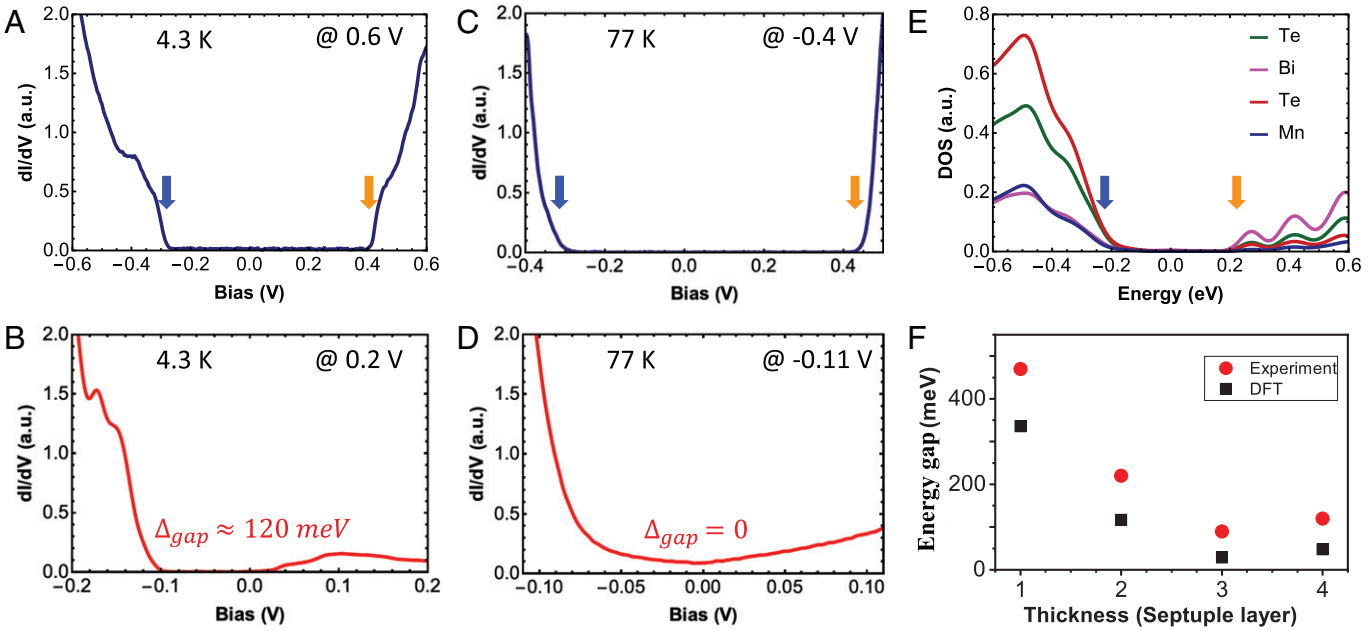

Fig. 2. Direct observation of Dirac mass gap. (*A* and *B*) STS taken on 4-SL $MnBi_2Te_4$ at 4.3 K with 0.6V and 0.2V setpoint biases. STS in *B* shows an ~120 *meV* Dirac mass gap. (*C* and *D*) STS taken on 4-SL $MnBi_2Te_4$ at 77 K with −0.4V and −0.11V setpoint biases. STS in *D* shows that the Dirac mass gap has disappeared. (*E*) DFT-calculated DOS for 4-SL $MnBi_2Te_4$ with a projection to the topmost four atomic layers. Blue and orange arrows in *A*, *C*, and *E* mark the threshold energies that bound the low-conductance bias region. a.u. stands for arbitrary unit. (*F*) Summarized STS-measured and DFT-calculated energy gap as a function of film thickness.

(Fig. 2*C*), the spectrum exhibits a low-conductance region from −0.3 V to 0.4 V, similar to that acquired in Fig. 2*A*. With a low setpoint bias (Fig. 2*D*), the electronic states near the Fermi level can be clearly observed. However, the gap disappears. This direct comparison further affirms that the observed gap at 4.3 K is the Dirac mass gap due to the exchange interaction of the Dirac surface states with the spontaneous magnetization below the Neel temperature.

Fig. 2*E* shows theoretical projected DOS curves for the top four atomic layers of a defect-free, 4-SL $MnBi_2Te_4$ thin film. These results show an ~0.45 eV low DOS energy range (marked between the blue and orange arrows), in agreement with our experimental observed low-conductance region of 0.7 eV. The true theoretical Dirac mass gap within which the DOS vanishes is only 48 meV for a 4-SL film. Fig. 2*F* summarizes the STS-measured (See *SI Appendix*, Fig. S4 for 1- to 3-SL STS) and the density functional theory (DFT)-calculated (*SI Appendix*, Fig. S5) energy gaps as a function of the film thickness, which shows excellent overall agreement, given the known tendency toward bandgap under-estimation in DFT. Our gap determinations have been cross-checked by obtaining STS data at different temperatures and in several different measurement modes (*SI Appendix*, Figs. S2 and S3). This provides unambiguous evidence of the Dirac mass gap in intrinsic MTIs, resolving current debates (9, 21, 23–28).

Role of Magnetic Antisite Defects

The thickness-dependent STS measurements discussed above were carried out in low defect areas, where STS shows consistent uniform gap values. We next discuss how defects impact the local electronic structure. Fig. 3*A* shows a region with low Mn_{Bi} antisites (<4%) on 4-SL $MnBi_2Te_4$. Fig. 3*B* displays spatial-dependent tunneling spectra. Depending on their specific locations, the tunneling peak features show intensity variation. However, the spectra exhibit a uniform gap value with E_F located within the gap. Note that the intrinsic nature of this sample suggests a similar amount of Bi_{Mn} antisite (n-type dopant) and Mn_{Bi} antisite (p-type dopant). This situation changes drastically in high defective areas. Fig. 3*C* shows the atomic image of the defective area on 3-SL $MnBi_2Te_4$, exhibiting high concentrations of Mn_{Bi} (~9%). In such areas, locally "defect-free" regions on the scale of 2 nm by 4 nm can be found. Fig. 3*D* shows a sequence of spectra from points between the locally defect-free region (position No. 1) and the defective area. The spectrum at position No. 1 exhibits a finite Dirac gap, whose tunneling features are similar to those on the clean area (*SI Appendix*, Fig. S4*C*). As one progresses to a defective area, the Dirac gap decreases (position No. 2) and eventually collapses (No. 3 to No. 6) with a V-shape DOS suggesting the recovery of the linear Dirac dispersion. Interestingly, in the spectra acquired in the defective region (No. 3 to No. 6), one observes an additional zero-bias anomaly, characterized by a dip at zero bias and two peaks at ±6 *meV*. We attribute this zero-bias anomaly to inelastic scattering due to spin excitations, similar to those reported previously in other systems (41–43), further confirming the magnetic nature of the Mn_{Bi} antisites. The evolution of the Dirac mass gap observed here strongly suggests the significance of defects concentration, particularly magnetic antisites, in suppressing the exchanging coupling between the Dirac surface states and the magnetic moments.

Ab Initio DFT and Coupled Dirac Cone Model Calculations

Motivated by our experimental observations, we performed DFT supercell calculation to account for the role of defects and interpreted them using a simplified Dirac-cone model (22) of the $MnBi_2Te_4$ electronic structure. Fig. 4*A* illustrates the magnetic moments and exchange couplings present in our model calculation. The Mn_{Bi} antisites moments have been shown to be antiparallel to those in the central Mn layer (31). Exchange interactions between Fermi-level electrons and these moments

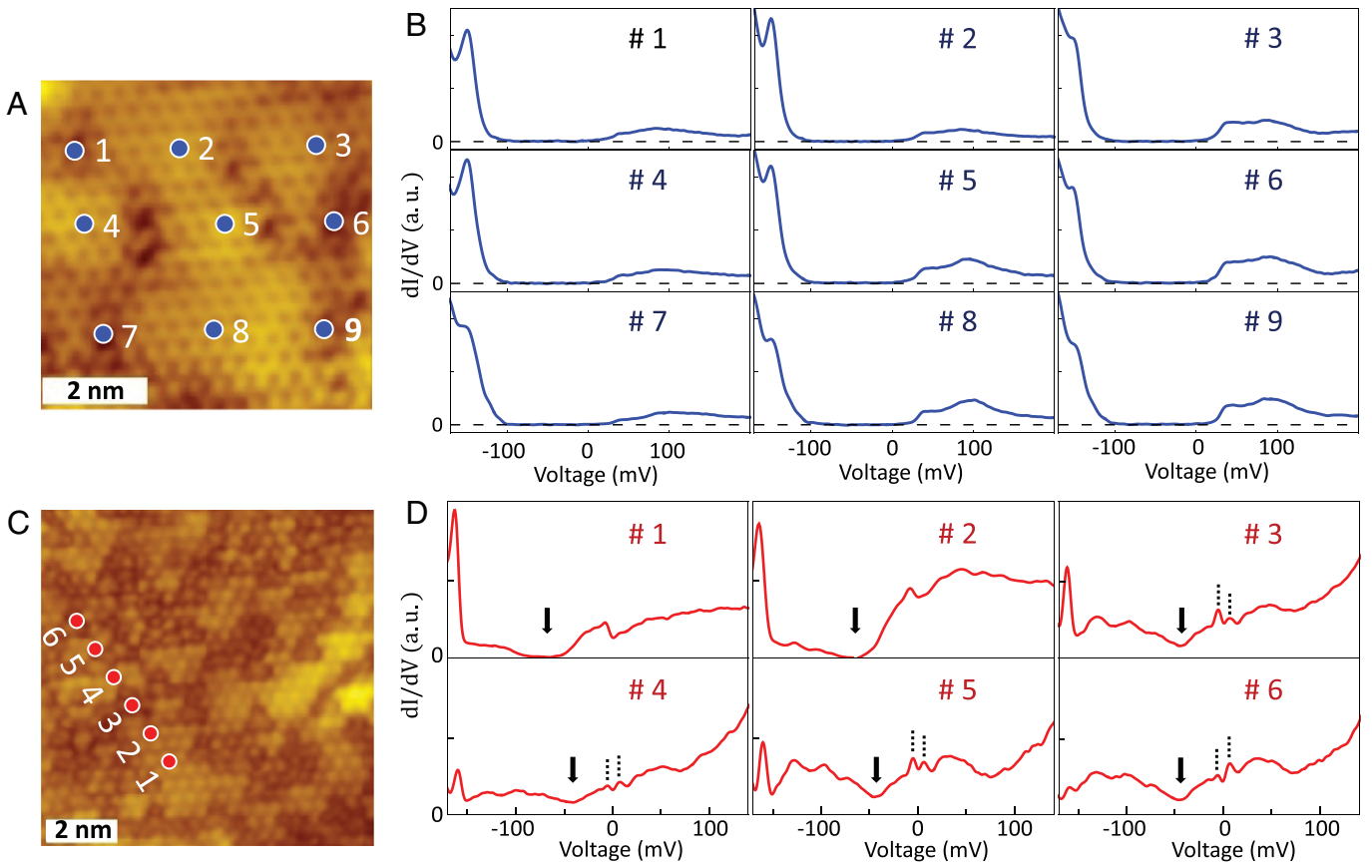

Fig. 3. Dirac mass gap variation as a function of defect distribution. (*A*) Atomic image taken on low-defect 4-SL region (setpoint bias: 0.3 *V*). (*B*) Spatial-dependent STS distribution with spatial locations marked in *A*. Horizontal black dashed lines mark zero. (*C*) Atomic image taken on high-defect 3-SL region (setpoint bias: −0.35 *V*). (*D*) Spatial-dependent STS distribution with spatial locations marked in *C*. Black arrows mark the Dirac point. Vertical black dashed lines on STS No. 3 to No. 6 mark the zero-bias tunneling anomaly.

partially cancel those from the central Mn layer, reducing the same-layer and neighboring-layer exchange couplings J_s and J_D (see *SI Appendix*, Fig. S6 for detailed definition.). To estimate the change of J_s and J_D as a function of magnetic antisites density, we perform DFT supercell calculations for bulk $MnBi_2Te_4$ crystals that have a ferromagnetic spin configuration and varying antisite defect configurations. A $4\times4\times1$ superstructure with one Mn_{Bi} antisite per 16 Bi atoms is used to simulate 6% Mn_{Bi} (see *SI Appendix*, Fig. S7 for more superstructure configuration information). To keep the chemical potential within the gap, we choose to compensate the Mn_{Bi} antisite with a Bi_{Mn} antisite by substituting the Bi atom with its next nearest-neighbor Mn atom, as illustrated in Fig. 4*A*. This antisite pair configuration has the lowest formation energy (31). The presence of Bi_{Mn} antisites also decreases J_S by reducing the magnetic moment in the Mn layer. As shown in Fig. 4*B*, bulk $MnBi_2Te_4$ with a ferromagnetic spin configuration is a topological Weyl semimetal (red curve). This topological phase is destroyed by 6% Mn_{Bi}, leading to a trivial insulating state (black curve).

We also calculate other defect concentrations to learn the evolution of electronic structure as defect density varies. Fig. 4*C* (red curve) summarizes the DFT-calculated Γ point energy gap as a function of defect density, showing a gap closing at around 2% Mn_{Bi}, at which a topological phase transition from a Weyl semimetal to a trivial insulator occurs, and illustrating the sensitivity of the topological phase of ferromagnetic bulk $MnBi_2Te_4$ to Mn_{Bi} concentration. Following a procedure similar to that employed in ref. (22), key model parameters, such as the exchange potential strength m_F, which is equal to sums and differences of J_S and J_D in the ferromagnetic and antiferromagnetic configurations, can be readily extracted from parallel-spin-configuration DFT energy bands. Fig. 4*C* (blue curve) plots the defect density dependence of m_F, showing that it decreases nearly linearly with an increase of defect density. In Fig. 4*C*, we normalize m_F relative to the same-layer and adjacent-layer Dirac cone hybridization parameters Δ_s and Δ_D (a detailed explanation of these parameters can be found in *SI Appendix*, Fig. S6).

Using the parameters extracted from DFT, we performed coupled Dirac cone model calculations for thin films with antiferromagnetic spin configurations. Fig. 4*D* summarizes the calculated Γ point energy gaps for both spin-aligned bulk and antiferromagnetic thin film cases. The bulk results (dashed black line) agree well with the DFT results (gold diamonds), confirming the validity of our model. For antiferromagnetic thin films, such as 4 and 6 SLs, gaps can be suppressed by half with less than 6% Mn_{Bi}. As is expected (44) (see *SI Appendix*, Fig. S8 for detailed discussion), this effect is even more dramatic for odd SLs, as exemplified by the 3 and 5 SLs results in Fig. 4*D*. In that case, gap values show a linear dependence on the defect density, and a topological phase transition occurs at around 1% for 3-SL and 6% for 5-SL thin films. A turning point occurs at about 9% due to the exchange coupling contributed by the Mn_{Bi} overtaking that by the central Mn layer. This eventually leads to a second gap crossing zero accompanied by a trivial insulator to Chern insulator transition with the opposite relationship between Chern number and magnetization. The gap-quenching defect concentration (1%) is small for

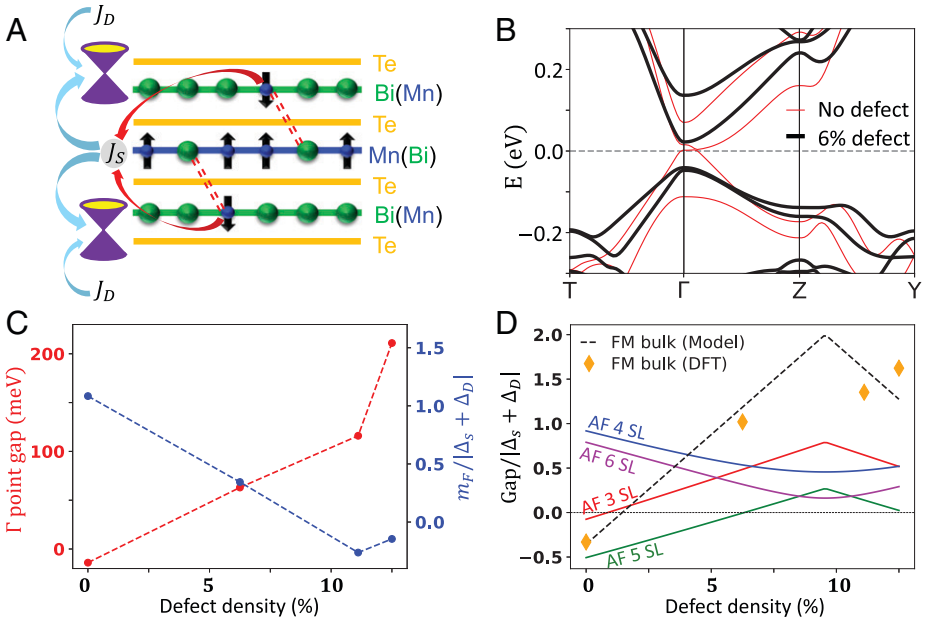

Fig. 4. *Ab initio* DFT calculation and coupled Dirac cone model. (*A*) Schematics for magnetic moments configuration and exchange couplings between the Dirac cones and the local magnetic moments. Both the Mn_{Bi} antisites and Mn layer contribute to the exchange coupling. Red dashed lines illustrate the next nearest-neighboring antisites pairs. (*B*) Calculated band dispersion for ferromagnetic bulk $MnBi_2Te_4$ in defect-free and 6% Mn_{Bi} antisites cases. (*C*) DFT-calculated Γ point energy gap and extracted model parameter m_F as a function of Mn_{Bi} antisites defect density. Negative gap values represent inverted bands. (*D*) Coupled Dirac cone model–calculated Γ point energy gap as a function of Mn_{Bi} antisites defect density in the case of ferromagnetic (FM) bulk and antiferromagnetic (AF) thin films. DFT-calculated FM bulk results are plotted in orange diamonds. FM (AF) refers to spin moments in Mn layers being aligned (antialigned) between adjacent SLs.

3-SL $MnBi_2Te_4$ in our model calculations because of accidental proximity to a topological phase transition (22). However, the experimental Dirac mass gap for 3 SLs is larger than that in the model calculation. Thus, its gap quenching should occur at a higher defect concentration.

This model captures the variation of the Dirac mass gap as the magnetic antisite density increases but neglects the antisite-induced disorder effect. In practice, observation of the QAH effect will require even lower Mn_{Bi} antisite densities than those predicted here. Current bulk $MnBi_2Te_4$ has a 3 to 6% Mn_{Bi} (26, 33, 39, 45) (10 to 20% of Mn_{Sb} for $MnSb_2Te_4$ (31, 32)) concentration. A large density of Bi_{Mn} antisites can also be inferred from the heavily degenerate n-type nature of the material. Considering the disorder effect, it is understandable why the QAH effect is not universally observed in an odd-SL $MnBi_2Te_4$ thin film (16, 17, 19, 20, 46).

Our experimental STM/S study of intrinsic MBE-grown $MnBi_2Te_4$ thin films provides unambiguous evidence for a Dirac mass gap in regions with low magnetic antisite defect density and resolves the current debate as to whether or not the topological surface states are gapped. STS spatial mapping across boundaries between pristine and defective regions directly reveals how Mn_{Bi} defects suppress the Dirac mass gap. *Ab initio* DFT and coupled Dirac cone model calculations unveil the microscopic mechanism for this correlation. The model calculations predict critical antisite densities above which the QAH effect cannot be observed in the antiferromagnetic $MnBi_2Te_4$ thin films (~6% for 5-SL films). By demonstrating the microscopic origin of the Dirac mass gap variation in $MnBi_2Te_4$, our work establishes magnetic defect as an important parameter in controlling the topological quantum phases.

Materials and Methods

Sample Growth and STM/S Measurements. $MnBi_2Te_4$ thin films were grown in a home-built MBE chamber with base pressure at ~10^{-10} Torr. HOPG substrates were cleaved in air and immediately transferred into the MBE chamber. HOPG substrates were outgassed at ~300 °C overnight before the growth of $MnBi_2Te_4$. High-purity Mn (99.99%), Bi (99.999%), and Te (99.999%) were evaporated from standard Knudsen cells. Samples were grown at 240 °C and postannealed at the growth temperature in a Te ambient. Samples were transferred from the MBE chamber into the STM chamber, with base pressure ~10^{-11} Torr, through a transfer vessel, with base pressure ~10^{-10} Torr, to maintain the cleanness of the film. STM/S measurements were conducted at 4.3 K. The W tip was prepared by electrochemical etching and then cleaned by *in situ* electron-beam heating. STM dI/dV spectra were measured using a standard lock-in technique with feedback loop off, whose modulation frequency is 490 Hz.

***Ab Initio* DFT Calculations.** DFT calculations were performed using Vienna *Ab Initio* Simulation Package (VASP) (47), in which generalized gradient approximations of Perdew–Burke–Ernzerhof (48) have been adopted for exchange-correlation potential. On-site correlation on the Mn 3d states is treated by performing a simplified (rotationally invariant) approach to the local-spin-density approximation + U calculations (49) with $U - J$ equals 5.34 eV. U and J represents the strength of the effective on-site Coulomb and exchange interactions. Twenty ångström of vacuum is used when calculating the $MnBi_2Te_4$ thin films to avoid the periodic image interactions normal to the surface. The global break condition for the electronic self-consistency loop is set to be 10^{-7} eV, and the plane wave energy cutoff is set to be 600 eV. DOSs in Fig. 2*E* are calculated on a 16 × 16 × 1 Γ-centered k-point integration grid with a Gaussian broadening factor of 50 meV.

Supercells that correspond to 3 × 3 × 1 and 4 × 4 × 1 of the original primitive cell were used to simulate the antisite defects in the ferromagnetic configuration. As illustrated in *SI Appendix*, Fig. S7, one Mn_{Bi} antisite per 16 Bi atoms in a 4 × 4 × 1 supercell corresponds to Mn_{Bi} density of 1/16, one Mn_{Bi} antisite per nine Bi atoms in a 3 × 3 × 1 supercell corresponds to Mn_{Bi} density of 1/9, and two Mn_{Bi} antisites per 16 atoms in a 4 × 4 × 1 supercell corresponds to Mn_{Bi} density of 1/8. The global break condition for the electronic self-consistency loop is set to be 10^{-6} eV, and a 9 × 9 × 3 Γ-centered k-point integration grid was employed.

Data, Materials, and Software Availability. All data are included in the manuscript and/or *SI Appendix*.

ACKNOWLEDGMENTS. This work was primarily supported by the NSF through the Center for Dynamics and Control of Materials: an NSF Materials Research Science and Engineering Centers under cooperative agreement no. DMR-1720595 and the US Air Force grant no. FA2386-21-1-4061. Other supports were from NSF grant nos. DMR-1808751, DMR-2219610, and the Welch Foundation F-1672. Work at Oak Ridge National Laboratory was supported by the US Department of Energy, Office of Science, Basic Energy Sciences, Materials Sciences and Engineering Division. We thank C.Z. Chang and Y.F. Zhao for the helpful discussion on MBE growth.

Author affiliations: [a]Department of Physics, The University of Texas at Austin, Austin, TX 78712; and [b]Materials Science and Technology Division, Oak Ridge National Laboratory, Oak Ridge, TN 37831

1. R. Li, J. Wang, X.-L. Qi, S.-C. Zhang, Dynamical axion field in topological magnetic insulators. *Nat. Phys.* **6**, 284–288 (2010).
2. R. S. K. Mong, A. M. Essin, J. E. Moore, Antiferromagnetic topological insulators. *Phys. Rev. B* **81**, 245209 (2010).
3. Y. Tokura, K. Yasuda, A. Tsukazaki, Magnetic Topological Insulators. *Nat. Rev. Phys.* **1**, 126 (2019).
4. R. Yu *et al.*, Quantized anomalous Hall effect in magnetic topological insulators. *Science* **329**, 61–64 (2010).
5. C.-Z. Chang *et al.*, Experimental observation of the quantum anomalous Hall effect in a magnetic topological insulator. *Science* **340**, 167–170 (2013).
6. I. Lee *et al.*, Imaging Dirac-mass disorder from magnetic dopant atoms in the ferromagnetic topological insulator $Cr_x(Bi_{0.1}Sb_{0.9})_{2-x}Te_3$. *Proc. Natl. Acad. Sci. U.S.A.* **112**, 1316–1321 (2015).
7. Y. S. Hor *et al.*, Development of ferromagnetism in the doped topological insulator $Bi_{2-x}Mn_xTe_3$. *Phys. Rev. B* **81**, 195203 (2010).
8. M. M. Otrokov *et al.*, Highly-ordered wide bandgap materials for quantized anomalous Hall and magnetoelectric effects. *2D Mater.* **4**, 025082 (2017).
9. M. M. Otrokov *et al.*, Prediction and observation of an antiferromagnetic topological insulator. *Nature* **576**, 416–422 (2019).
10. J. Li *et al.*, Intrinsic magnetic topological insulators in van der Waals layered $MnBi_2Te_4$-family materials. *Sci. Adv.* **5**, eaaw5685 (2019).
11. W. Ning, Z. Mao, Recent advancements in the study of intrinsic magnetic topological insulators and magnetic Weyl semimetals. *APL Mater.* **8**, 090701 (2020).
12. C. Hu *et al.*, A van der Waals antiferromagnetic topological insulator with weak interlayer magnetic coupling. *Nat. Commun.* **11**, 97 (2020).
13. C. Liu *et al.*, Robust axion insulator and Chern insulator phases in a two-dimensional antiferromagnetic topological insulator. *Nat. Mater.* **19**, 522–527 (2020).
14. J. Ge *et al.*, High-Chern-number and high-temperature quantum Hall effect without Landau levels. *Natl. Sci. Rev.* **7**, 1280–1287 (2020).
15. Y. Deng *et al.*, Quantum anomalous Hall effect in intrinsic magnetic topological insulator $MnBi_2Te_4$. *Science* **367**, 895–900 (2020).
16. Y.-F. Zhao *et al.*, Even-odd layer-dependent anomalous hall effect in topological magnet $MnBi_2Te_4$ thin films. *Nano Lett.* **21**, 7691–7698 (2021).
17. L. Tai *et al.*, Distinguishing two-component anomalous Hall effect from topological Hall effect in magnetic topological insulator $MnBi_2Te_4$. *arXiv* [Preprint] arXiv: 2103.09878 (2021).
18. J. Cui *et al.*, Transport properties of thin flakes of the antiferromagnetic topological insulator MnBi2Te4. *Phys. Rev. B* **99**, 155125 (2019).
19. D. Ovchinnikov *et al.*, Intertwined topological and magnetic orders in atomically thin Chern insulator $MnBi_2Te_4$. *Nano Lett.* **21**, 2544–2550 (2021).
20. C. Liu *et al.*, Magnetic-field-induced robust zero Hall plateau state in $MnBi_2Te_4$ Chern insulator. *Nat. Commun.* **12**, 4647 (2021).
21. M. M. Otrokov *et al.*, Unique thickness-dependent properties of the van der Waals interlayer antiferromagnet $MnBi_2Te_4$ films. *Phys. Rev. Lett.* **122**, 107202 (2019).
22. C. Lei, S. Chen, A. H. MacDonald, Magnetized topological insulator multilayers. *Proc. Natl. Acad. Sci. U.S.A.* **117**, 27224–27230 (2020).
23. Y. J. Chen *et al.*, Topological electronic structure and its temperature evolution in antiferromagnetic topological insulator $MnBi_2Te_4$. *Phys. Rev. X* **9**, 041040 (2019).
24. Y.-J. Hao *et al.*, Gapless surface dirac cone in antiferromagnetic topological insulator $MnBi_2Te_4$. *Phys. Rev. X* **9**, 041038 (2019).
25. X. Wu *et al.*, Distinct topological surface states on the two terminations of $MnBi_4Te_7$. *Phys. Rev. X* **10**, 031013 (2020).
26. Y. Yuan *et al.*, Electronic states and magnetic response of $MnBi_2Te_4$ by scanning tunneling microscopy and spectroscopy. *Nano Lett.* **20**, 3271–3277 (2020).
27. P. M. Sass, J. Kim, D. Vanderbilt, J. Yan, W. Wu, Robust A-type order and spin-flop transition on the surface of the antiferromagnetic topological insulator $MnBi_2Te_4$. *Phys. Rev. Lett.* **125**, 037201 (2020).
28. Z. Liang *et al.*, Mapping Dirac fermions in the intrinsic antiferromagnetic topological insulators $(MnBi_2Te_4)(Bi_2Te_3)_n$ (n=0,1). *Phys. Rev. B* **102**, 161115 (2020).
29. D. Nevola *et al.*, Coexistence of surface ferromagnetism and a gapless topological state in $MnBi_2Te_4$. *Phys. Rev. Lett.* **125**, 117205 (2020).
30. B. Li *et al.*, Competing magnetic interactions in the antiferromagnetic topological insulator $MnBi_2Te_4$. *Phys. Rev. Lett.* **124**, 167204 (2020).
31. Y. Lai, L. Ke, J. Yan, R. D. McDonald, R. J. McQueeney, Defect-driven ferrimagnetism and hidden magnetization in $MnBi_2Te_4$. *Phys. Rev. B* **103**, 184429 (2021).
32. Y. Liu *et al.*, Site mixing for engineering magnetic topological insulators. *Phys. Rev. X* **11**, 021033 (2021).
33. M. Garnica *et al.*, Native point defects and their implications for the Dirac point gap at $MnBi_2Te_4$(0001). *NPJ Quantum Mater.* **7**, 7 (2022).
34. T. Hirahara *et al.*, Large-gap magnetic topological heterostructure formed by subsurface incorporation of a ferromagnetic layer. *Nano Lett.* **17**, 3493–3500 (2017).
35. E. D. L. Rienks *et al.*, Large magnetic gap at the Dirac point in $Bi_2Te_3/MnBi_2Te_4$ heterostructures. *Nature* **576**, 423–428 (2019).
36. S. Wimmer *et al.*, Mn-Rich $MnSb_2Te_4$: A topological insulator with magnetic gap closing at high curie temperatures of 45-50 K. *Adv. Mater.* **33**, e2102935 (2021).
37. P. Küppers *et al.*, Probing the magnetic band gap of the ferromagnetic topological insulator MnSb2Te4. *arXiv* [Preprint] *arXiv:2202.11540* (2021).
38. D. S. Lee *et al.*, Crystal structure, properties and nanostructuring of a new layered chalcogenide semiconductor, Bi_2MnTe_4. *CrystEngComm* **15**, 5532 (2013).
39. Z. Huang, M.-H. Du, J. Yan, W. Wu, Native defects in antiferromagnetic topological insulator MnBi2Te4. *Phys. Rev. Mater.* **4**, 121202 (2020).
40. M. H. Du, J. Yan, V. R. Cooper, M. Eisenbach, Tuning fermi levels in intrinsic antiferromagnetic topological insulators $MnBi_2Te_4$ and $MnBi_4Te_7$ by defect engineering and chemical doping. *Adv. Funct. Mater.* **31**, 2006516 (2021).
41. A. A. Khajetoorians *et al.*, Detecting excitation and magnetization of individual dopants in a semiconductor. *Nature* **467**, 1084–1087 (2010).
42. A. A. Khajetoorians *et al.*, Spin excitations of individual Fe atoms on Pt(111): impact of the site-dependent giant substrate polarization. *Phys. Rev. Lett.* **111**, 157204 (2013).
43. C. F. Hirjibehedin, C. P. Lutz, A. J. Heinrich, Spin coupling in engineered atomic structures. *Science* **312**, 1021–1024 (2006).
44. C. Lei, A. H. MacDonald, Gate-tunable quantum anomalous Hall effects in MnBi2Te4 thin films. *Phys. Rev. Mater.* **5**, L051201 (2021).
45. J.-Q. Yan *et al.*, Crystal growth and magnetic structure of MnBi2Te4. *Phys. Rev. Mater.* **3**, 064202 (2019).
46. J. Yan, The elusive quantum anomalous Hall effect in MnBi2Te4: a materials perspective. *arXiv* [Preprint] *arXiv:2112.09070* (2021).
47. G. Kresse, J. Hafner, Ab initio molecular dynamics for liquid metals. *Phys. Rev. B Condens. Matter* **47**, 558–561 (1993).
48. J. P. Perdew, K. Burke, M. Ernzerhof, Generalized gradient approximation made simple. *Phys. Rev. Lett.* **77**, 3865–3868 (1996).
49. B. Himmetoglu, A. Floris, S. de Gironcoli, M. Cococcioni, Hubbard-corrected DFT energy functionals: The LDA+U description of correlated systems. *Int. J. Quantum Chem.* **114**, 14–49 (2014).